

Extreme surface and near-bottom currents in the northwest Atlantic

Eric C. J. Oliver · Jinyu Sheng · Keith R. Thompson ·
Jorge R. Urrego Blanco

Received: 25 March 2012 / Accepted: 12 July 2012
© Springer Science+Business Media B.V. 2012

Abstract This study presents a methodology for estimating extreme current speeds from numerical model results using extremal analysis techniques. This method is used to estimate the extreme near-surface and near-bottom current speeds of the northwest Atlantic Ocean with 50-year return periods from 17 years of model output. The non-tidal currents produced by a three-dimensional ocean circulation model for the 1988–2004 period were first used to estimate and map the 17-year return period extreme current speeds at the surface and near the bottom. Extremal analysis techniques (i.e., fitting the annual maxima to the Type I probability distribution) are used to estimate and map the 50-year extreme current speeds. Tidal currents are dominant in some parts of the northwest Atlantic, and a Monte Carlo-based methodology is developed to take into account the fact that large non-tidal extrema may occur at different tidal phases. The inclusion of tidal currents in this way modifies the estimated 50-year extreme current speeds, and this is illustrated along several representative transects and depth profiles. Seasonal variations are examined by calculating the extreme current speeds for fall-winter and spring–summer. Finally, the distribution of extreme currents is interpreted taking into account (1) variability about the time-mean current speeds, (2) wind-driven Ekman currents, and (3) flow along isobaths.

Keywords Extreme current speeds · Extremal analysis · Northwest Atlantic · Ocean circulation model · Monte Carlo methods

1 Introduction

The estimation of extreme ocean currents is of interest from both a scientific point of view as well as for practical applications. Scientifically, understanding when and where extreme currents occur provides information on the probability distribution of the ocean state as

E. C. J. Oliver (✉) · J. Sheng · K. R. Thompson · J. R. U. Blanco
Department of Oceanography, Dalhousie University, Halifax, NS, Canada
e-mail: eric.oliver@utas.edu.au

Present Address:

E. C. J. Oliver
Institute for Marine and Antarctic Studies, University of Tasmania, Hobart, TAS, Australia

well as insight into its dynamics. For example, how does the distribution of extreme currents relate to the mean circulation pattern? What roles do the mean flow or atmospheric forcing conditions play in driving extreme surface currents? From a practical standpoint, extreme surface and bottom currents are important in marine engineering. For example, when designing and insuring offshore oil platforms or subsurface pipelines, it is important to have estimates of what extreme conditions might be experienced by these devices.

The region chosen for this study is the northwest Atlantic that is a major shipping and fishing area and more recently is being explored and developed by the oil and gas industries. These activities could benefit from a better understanding of extreme ocean conditions in the region, and there are presently only a few relevant studies in the literature. Bernier and Thompson (2006) and Bernier et al. (2007) analyzed and mapped extreme sea levels in the northwest Atlantic. They applied statistical methods to predict extreme sea levels with 40-year return periods but did not examine extreme current speeds. Wu et al. (2011) examined extreme currents from a regional general circulation model forced by historical storms. They estimated the maximum surface and near-bottom currents, for 22 realistic storms, over the Grand banks and surrounding areas. These authors, however, did not model the extremes statistically or attempt predictions of extreme currents for long return periods.

Most of the previous application of extremal analysis to oceanographic data have focused on extreme sea level (e.g., Pugh and Vassie 1980; Tawn and Vassie 1989; Tawn 1992; Dixon et al. 1998). Relatively few studies have focused on extreme ocean currents (e.g., Pugh 1982; Carter et al. 1987; Griffiths 1996), primarily due to the lack of long records of ocean currents but also the bivariate nature of ocean currents, which complicates any extremal analysis. Fortunately, there is a large body of analogous work on modeling extreme winds (e.g., Hennessey 1977; Cook 1985; Zwiers 1987; Coles and Walshaw 1994), and a good review of the methods used in those studies can be found in Palutikof et al. (1999). The present work aims to describe extreme current speeds in the northwest Atlantic by extending the previous analyses of Bernier and Thompson (2006), Bernier et al. (2007), and Wu et al. (2011). We describe a straightforward methodology for estimating long-period extreme ocean currents using extreme analysis techniques applied to modeled ocean current time series of a length shorter than typical return periods required for insurance and design considerations (e.g., 50–100 years or longer). The focus of this study is extreme currents over the shelf and slope regions although some deep water results are also discussed.

In this study, we have used predictions of ocean currents over the 1988–2004 period and extremal analysis techniques to estimate extreme surface and near-bottom current speeds in the northwest Atlantic. The current predictions, along with an outline of the extremal analysis techniques, are presented in Sect. 2. The time-mean current speeds and the maximum current speeds are then mapped (Sects. 3.1 and 3.2 respectively), and 50-year extreme current speeds are then estimated using extremal analysis (Sect. 3.3). In some regions, tides are important and they are shown to significantly alter estimates of the 50-year extreme current speeds (Sect. 4) The distribution of extreme currents is interpreted by taking into account the time-mean current speeds, wind-forced Ekman currents, and the steering of flow along isobaths (Sect. 5). The summary and discussion are presented in Sect. 6.

2 Predictions of northwest Atlantic currents

The horizontal ocean currents (\mathbf{u}) were decomposed into a sum of tidal (\mathbf{u}^T) and non-tidal (\mathbf{u}^{NT}) components in order to obtain more realistic statistical estimates of extreme currents

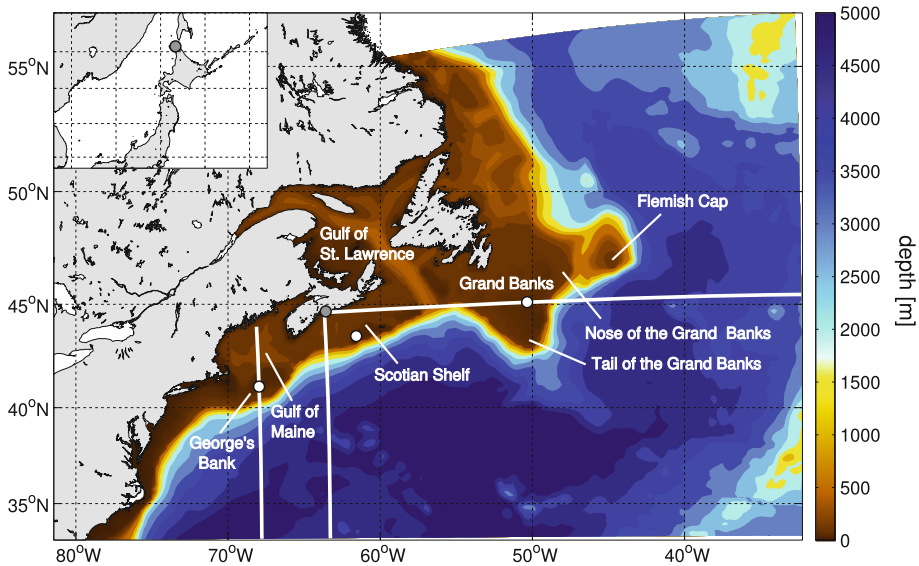


Fig. 1 The domain and bathymetry of the northwest Atlantic used by the ocean circulation model. The grid size is about $1/4^\circ$. The white lines show the transects, and the white circles show the depth profile locations, used in Sect. 4 The two gray circles show the locations of the Halifax and Wakkanaï tide gauges used in “Appendix 2”

(the non-linear interaction between the tidal and non-tidal components was ignored in this study). Predictions of non-tidal currents in the northwest Atlantic were made by a regional ocean circulation model, and predictions of tidal currents were provided by a tidal prediction model, as detailed below.

The non-tidal ocean currents (u^{NT}) were hindcast over the 1988–2004 period using a coupled ocean-ice numerical model developed recently by Urrego-Blanco and Sheng (2012). The model domain covers the northwest Atlantic Ocean from 33°N to 55°N and 80°W to 33°W (Fig. 1). The model is described in more detail in “Appendix 1”. The model provides 6-h instantaneous predictions of non-tidal currents. The “surface” currents are taken from the center of the uppermost model z -level (3 m depth) and “near-bottom” currents are taken from the center of the lowest model z -level. The depth of the near-bottom currents varies with location from 3 to 10 m over the shallowest regions (e.g., George’s Bank, the Scotian Shelf, the Grand Banks, most of the Gulf of St. Lawrence), to 20–50 m in some of the deeper portions of the continental shelf (e.g., the Gulf of Maine, the Laurentian Channel) and along the shelf break. The depth of the near-bottom currents is up to 125 m in most of the open ocean.

The amplitude A_i and phase θ_i of zonal and meridional barotropic tidal currents, where i represents the tidal constituent of interest, were produced by a simple tidal prediction program known as WebTide based on precalculated harmonic constants of major tidal constituents (Lyard et al. 2006). In general, A_i and θ_i are dependent on latitude and longitude. Tidal currents (u^T) are then calculated as the following sum over all constituents:

$$u_i^T = \sum_i A_i^{(u)} \cos(\omega_i t + \theta_i^{(u)}) \tag{1}$$

$$v_t^T = \sum_i A_i^{(v)} \cos(\omega_i t + \theta_i^{(v)}), \quad (2)$$

where ω_i is the frequency of the i th tidal constituent. In this study, we used only the following eight tidal constituents: M2, K1, N2, S2, O1, M3, M4, and M6. The tidal currents are assumed constant throughout the water column at the depth-averaged value, that is, the surface and near-bottom tidal currents are simply equal to depth-averaged value.

The methodology used to estimate extreme non-tidal current speeds consists of fitting the Gumbel (Type I) probability distribution to the current speed annual maxima and extrapolating to the desired return period (see “Appendix 2”). The effect of tidal currents is taken into account using a Monte Carlo approach that also allows for more accurate predictions of extreme currents with long return periods (see “Appendix 3”). These methods have been validated in those Appendices using long sea level records from Halifax (Canada), which is tidally dominant, and Wakkanai (Japan), which is not tidally dominant.

3 Extreme non-tidal current speeds

The time-mean (non-tidal) current speeds produced by the couple ice-ocean model in the northwest Atlantic are first presented here followed by estimates of extreme non-tidal current speeds. More details on the model results can be found in Urrego-Blanco and Sheng (2012).

3.1 Simulated mean current speeds

We first examine $\overline{|\mathbf{u}^{\text{NT}}|}$ which is defined as the time-mean of the hindcast current speeds produced by the model. At the surface, the mean speed is dominated by the major current systems in the region including the Gulf Stream and the Labrador Current (Fig. 2, upper panel). In general, the numerical model reproduces well the observed time-mean circulation (see Loder et al. (1998) for a review of the oceanography in this region; see Urrego-Blanco and Sheng (2012) for more details on the performance and validation of the numerical model). The Gulf Stream flows along the Atlantic coast of the United States with speeds exceeding 0.5 m/s and separates just north of Cape Hatteras. The signature of the North Atlantic Current is evident south and east of the Grand Banks with speeds of up to 0.5 m/s. The Labrador Current flows south from the northern open boundary with speeds of up to 0.35 m/s, and both the inshore and offshore branches are clearly visible. Flow around steep topography is also evident (e.g., around the Grand Banks, the Flemish Cap, the Scotian Shelf, and the Laurentian Channel).

The near-bottom mean current speeds, calculated from currents in the lowest model z -level, forms a more complex pattern than at the surface (Fig. 2, lower panel). Signatures of the Gulf Stream and the offshore branch of the Labrador Current are no longer dominant in the near-bottom circulation. Flow is now strongest (over 0.2 m/s) in areas of steep topography such as the edges of the Grand Banks, the Flemish Cap, and the Scotian Shelf.

The mean speed also exhibits significant seasonal changes produced by the coupled ice-ocean model (not shown). Fall–winter is defined as September through February; spring–summer is defined as March through August. In general, mean current speeds are stronger in fall–winter than in spring–summer. This seasonality is most pronounced in the shallow regions of the Scotian Shelf, Gulf of St. Lawrence, and the Grand Banks where both surface and near-bottom currents are typically 0.1 m/s stronger in fall–winter. We explain

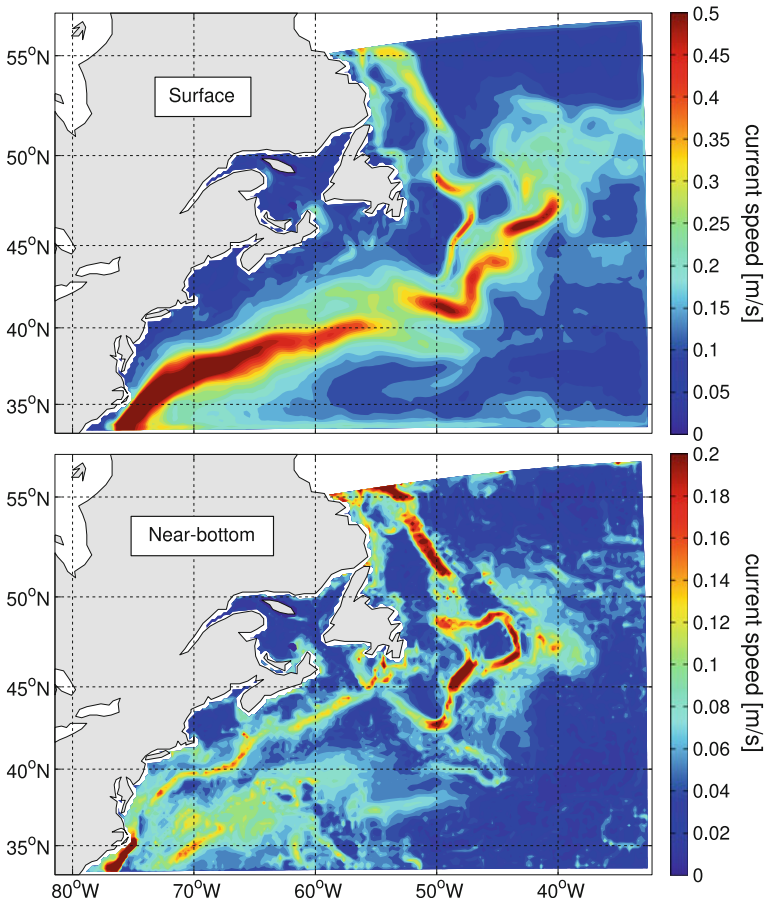


Fig. 2 Time-mean ocean current speeds, $|\overline{\mathbf{u}^{NT}}|$, in the northwest Atlantic calculated from the three-dimensional non-tidal currents produced by the coupled ice-ocean model. The non-tidal current speeds are shown at the surface (*top*) and near the bottom (*bottom*). Surface currents are at 3 m depth, and near-bottom currents are taken from the center of the bottom-most model z -level (see text for details)

this seasonal difference by the fact that surface winds are generally much stronger in fall–winter than in spring–summer.

3.2 Simulated maximum current speeds

We next examine the maximum current speed at each grid point $|\mathbf{u}^{NT}|_{\max}$, which provides an estimate of the 17-year extreme current speed (i.e., $|\mathbf{u}^{NT}|_{17}$) at that location. The pattern of maximum surface currents in spring–summer (Fig. 3, upper right) has similar horizontal structures as the mean current speed that is affected by major currents in the region including the Gulf Stream, the North Atlantic Current, etc. Maximum current speeds up to 2 m/s are present in the upper Gulf Stream with typical speeds of 1 m/s further downstream. Maximum current speeds are much weaker in the Labrador Current (less than 0.5 m/s), and there are currents up to 1 m/s around the steep topography of the Grand Banks. In fall–winter, this pattern is also evident along with extreme current speeds of up to 1 m/s in shallow areas

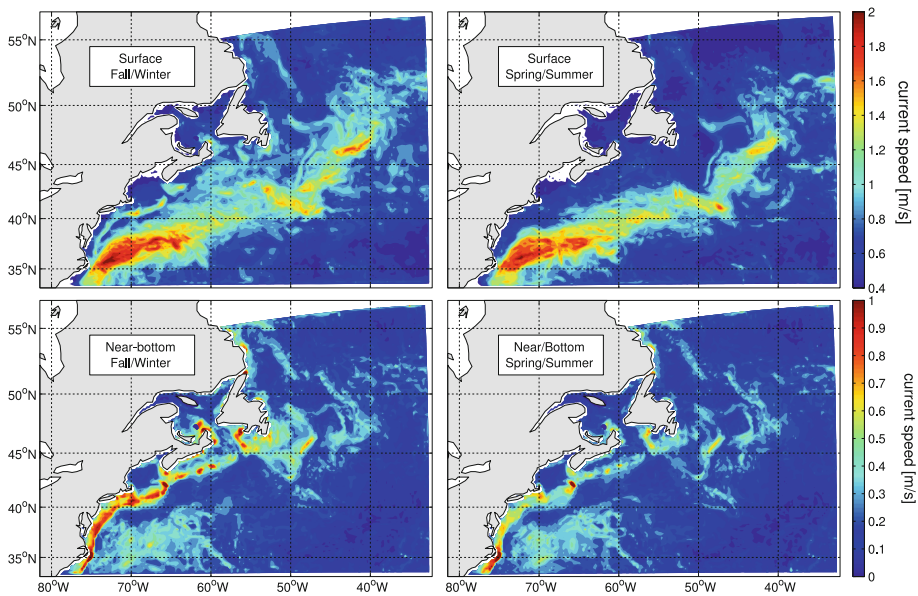


Fig. 3 Maximum non-tidal current speeds, $|\mathbf{u}^{\text{NT}}|_{\text{max}}$, in the northwest Atlantic for the 17-year simulation period (1988–2004). The maximum current speeds are shown for fall–winter (*left panels*) and spring–summer (*right panels*). The *upper and lower panels* are for the surface and near-bottom current speeds respectively

(Fig. 3, upper left) especially over the Grand Banks, the Scotian Shelf, and around Cape Breton Island. There is also a notable band of strong flow (up to 1.5 m/s) running along the Gulf of Maine shelf break that is not evident in spring–summer and may be due to wind-driven currents oriented along lines of constant bathymetry. Maximum speeds in the Labrador Current are also about twice as strong in fall–winter (about 1 m/s) than in spring–summer.

The distribution of maximum near-bottom currents (Fig. 3, lower panels) is not as well correlated with the time-mean flow pattern as the distribution of surface maximum surface currents. Extreme currents in areas of strong time-mean flow are still evident, such as in the Gulf Stream and along the continental slope, but most extreme currents are found over shallow regions. Speeds of 0.4–0.6 m/s are found over the Grand Banks, Scotian Shelf, and around Cape Breton Island in spring–summer (Fig. 3, lower right). Current speeds above 0.6 m/s are found along the continental shelf break further south. In fall–winter, near-bottom current speeds are larger in all shallow regions with values exceeding 1 m/s over St. Pierre Bank, around Cape Breton Island, and along the continental shelf break.

The magnitudes and geographic pattern of $|\mathbf{u}^{\text{NT}}|_{\text{max}}$ are largely consistent with the results of Wu et al. (2011). They found strong surface currents (up to 1.2 m/s) over the region affected by the North Atlantic Current, along the shelf break of the Grand Banks, and over St. Pierre Bank. Strong near-bottom currents (up to 0.4 m/s) were also found over St. Pierre Bank as well as over much of the Grand Banks, Scotian Shelf, and around Cape Breton Island.

3.3 Estimated 50-year extreme currents speeds

The extremal analysis method outlined in “Appendix 2” was applied to the time series of current speed annual maxima in the northwest Atlantic. The 50-year extreme current speed

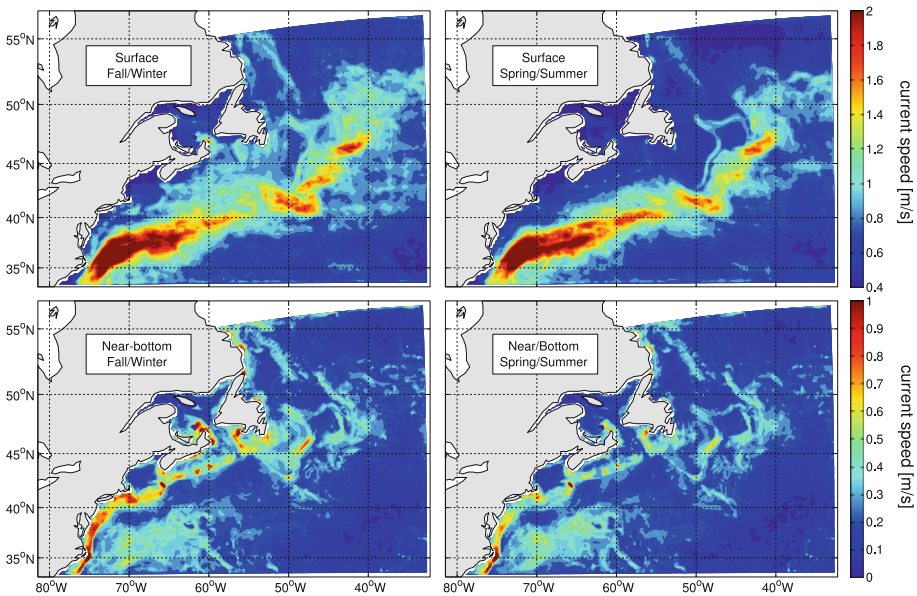


Fig. 4 Extreme non-tidal current speeds in the northwest Atlantic with a return period of 50 years, $|\mathbf{u}^{\text{NT}}|_{50}$. The extreme current speed, estimated from a fit of the non-tidal model current speed annual maxima to the Type I distribution, is shown for fall–winter (*left panels*) and spring–summer (*right panels*) at the surface (*upper panels*) and near the bottom (*lower panels*)

$|\mathbf{u}^{\text{NT}}|_{50}$ was estimated from the Type I distribution (see Eq. 5) fit to the 17 annual maxima calculated from the currents simulated by the coupled model (Fig. 4). Seasonal dependence of $|\mathbf{u}^{\text{NT}}|_{50}$ was examined by replacing the annual maxima by fall–winter maxima or spring–summer maxima prior to fitting the Type I distribution. We note that it has been suggested for wind speed, which may be considered analogous to ocean current speed, that a better fit is provided by fitting the Type I distribution to the square of the speeds (e.g., Cook 1985; Palutikof et al. 1999). However, we found the results were not strongly sensitive to this choice, and so for simplicity, we fit to the ocean current speed.

The distribution of $|\mathbf{u}^{\text{NT}}|_{50}$ is very similar to that of $|\mathbf{u}^{\text{NT}}|_{\text{max}}$ except for the higher magnitudes. The $|\mathbf{u}^{\text{NT}}|_{50}$ are typically 10–20 % stronger than the $|\mathbf{u}^{\text{NT}}|_{\text{max}}$. The $|\mathbf{u}^{\text{NT}}|_{50}$ are generally stronger in fall–winter than in spring–summer, consistent with the $|\mathbf{u}^{\text{NT}}|_{\text{max}}$. In some areas, including surface currents within the Gulf Stream, the $|\mathbf{u}^{\text{NT}}|_{50}$ are up to 35 % stronger in spring–summer and over 50 % stronger in fall–winter. This indicates that the dependence of extreme currents on return period is not uniform in space, that is, the parameters of the Type I distribution vary with geographic location.

4 The inclusion of tidal currents

The calculation of extreme current speeds presented in Fig. 4 does not include the influence of tidal currents that can be large, and even dominant, in some parts of the northwest Atlantic. In order to explore the relative importance of tidal and non-tidal currents, we have calculated the ratio of the total standard deviation of tidal current velocities to the total

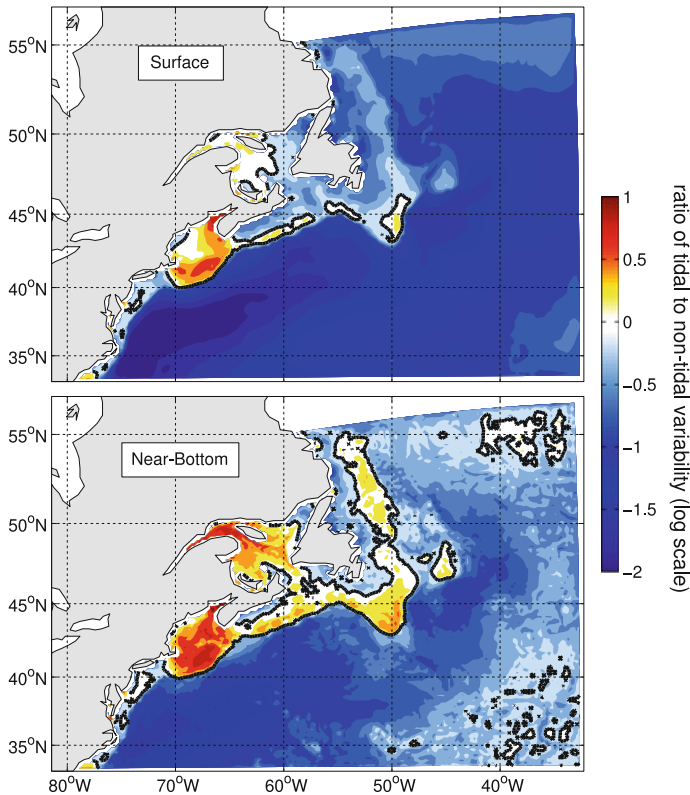


Fig. 5 Relative strength of tidal and non-tidal currents over the northwest Atlantic. Filled contours indicate the ratio of total standard deviation of tidal currents to total standard deviation of non-tidal currents at the surface (*top*) and near the bottom (*bottom*). The *thick black contour* denotes a ratio of one (i.e., tidal and non-tidal currents of equal strength)

standard deviation of non-tidal current velocities. Total standard deviation σ is defined as $\sigma = \sqrt{\sigma_u^2 + \sigma_v^2}$ where σ_u and σ_v are the standard deviations of u and v respectively.

Tidal currents dominate over large areas of the model domain especially in shallow regions (Fig. 5). Surface tidal currents are dominant in the Bay of Fundy/Gulf of Maine and parts of the Scotian Shelf, the Grand Banks, and the Gulf of St. Lawrence (Fig. 5, upper panel). Surface tidal currents are especially strong in the Bay of Fundy and the Gulf of Maine where they are nearly 10 times stronger than non-tidal currents. Near the bottom, the area over which tidal currents dominate extends to include all of the shallow areas mentioned above as well as the Flemish Cap and most of the Scotian Shelf, the Grand Banks, and the shallow regions off the northeast coasts of Newfoundland and Labrador (Fig. 5, lower panel). Near-bottom tidal currents are up to 10 times stronger in the Bay of Fundy and Gulf of Maine, the upper St. Lawrence Estuary, and the tail of the Grand Banks. The influence of wind forcing on ocean currents, which is one of major sources for non-tidal variability, is confined mainly in the surface mixed layer, which explains why the tidal currents are more dominant near the bottom than at the sea surface as shown in Fig. 5.

The relative importance of tidal and non-tidal currents has been calculated by season (not shown). The seasonal dependence is weak but in general non-tidal currents are more dominant in fall–winter than in spring–summer. Most notable is that the areas over which

non-tidal currents are dominant (i.e., blue areas in Fig. 5) are larger during fall–winter. This is due to the fact that non-tidal variability is stronger in fall–winter, especially in shallow areas, while the barotropic tidal variability does not change with season. Seasonal changes in stratification may have an impact on baroclinic tidal variability but we have not considered this possibility in the present study.

In the tidally dominant regions discussed above, the tidal currents must be included in the analysis in order to obtain realistic predictions of extreme currents. The simplest method would be to add tidal predictions to the non-tidal currents produced by the coupled model for the exact dates and times at which these currents are defined. However, tidal currents can vary significantly over a few hours, and the timing of the model currents (defined by the timing of the surface forcing) may not be accurate to this time scale. Therefore, we will use the Monte Carlo method described in “Appendix 3” to include the influence of tidal currents.

The Monte Carlo method was applied to surface and near-bottom current speeds for regions where the ratio of the total standard deviation of tidal current velocities to the total standard deviation of non-tidal current velocities is greater than one-third. The cutoff of one-third was chosen subjectively as the value above which the inclusion of tidal currents significantly influenced the predicted current speeds. In this way, extreme total current speeds with a return period of 50 years, $|u|_{50}$, were estimated (Fig. 6). At the surface, the inclusion of tides increased $|u|_{50}$ significantly over George’s Bank and around Cape Cod and southwestern Nova Scotia, as expected. Near the bottom, $|u|_{50}$ are also significantly

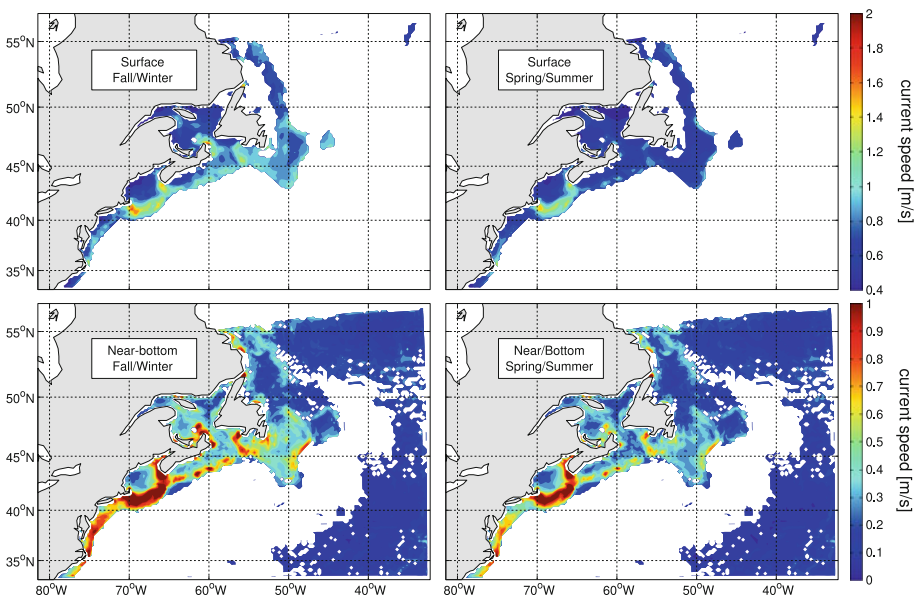


Fig. 6 Extreme current speeds in the northwest Atlantic, including the effect of tides, with a return period of 50 years, $|u|_{50}$. The extreme current speed, estimated from a fit of the non-tidal model current speed annual maxima to the Type I distribution, and applying the Monte Carlo method described in “Appendix 3”, is shown for fall–winter (left panels) and spring–summer (right panels) at the surface (upper panels) and near the bottom (lower panels). The extreme current speeds are only plotted for regions where the ratio of the total standard deviation of tidal current velocities to the total standard deviation of non-tidal current velocities (see Fig. 5) is greater than one-third

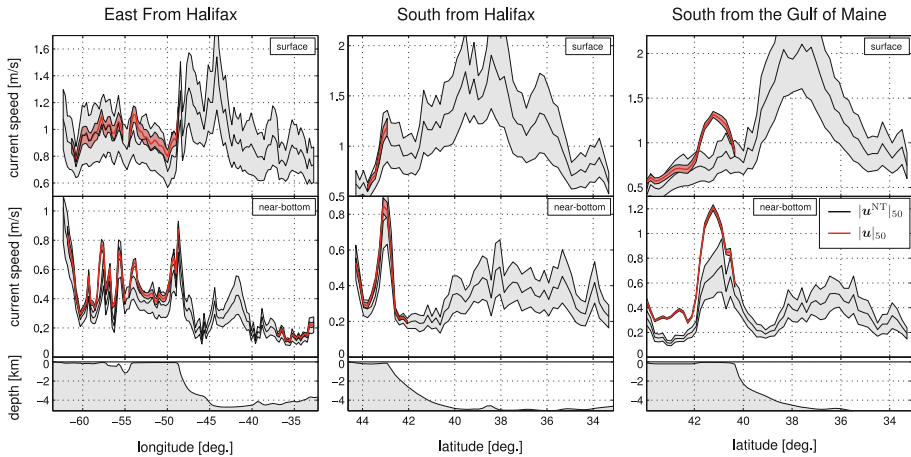


Fig. 7 Extreme currents along several transects with a return period of 50 years. The transects run east from Halifax (*left*), south from Halifax (*center*), and south from the Gulf of Maine (*right*). The transects are shown in Fig. 1. The 50-year extreme current speeds $|u^{NT}|_{50}$ (solid lines) and $|u|_{50}$ (dashed lines) are shown at the surface (top panels) and near the bottom (middle panels). The $|u|_{50}$ are only shown for regions where the standard deviation of tidal currents is at least one-third of the standard deviation of non-tidal currents. Shaded areas indicate the 95 % confidence intervals. The bathymetry along each transect is shown in the bottom panels

higher in these regions as well as in the Gulf of St. Lawrence and parts of the Scotian Shelf and the Grand Banks.

The same analysis was also applied to current speeds along three transects and for three vertical profiles. The three transects run east from Halifax, south from Halifax, and south from the Gulf of Maine (Fig. 1, white lines). The three depth profiles are located on George’s Bank, the Scotian Shelf, and the tail of the Grand Banks (Fig. 1, white circles). The $|u^{NT}|_{50}$ and $|u|_{50}$ along the three transects are shown in Fig. 7. The Monte Carlo method has only been applied in regions where the total standard deviation of the tidal currents is at least one-third of the total standard deviation of the non-tidal currents. The inclusion of tidal currents has a significant impact on the predicted extreme currents. This is especially true in shallow regions where the barotropic tides are amplified. For example, near-bottom extreme currents over George’s Bank are 60 % stronger once the influence of tidal currents is taken into account.

Depth profiles of $|u^{NT}|_{50}$ and $|u|_{50}$ at three locations are shown in Fig. 8. At each of these locations, the total standard deviation of the tidal currents is at least one-third of the total standard deviation of the non-tidal currents. Extreme currents are strongest at the surface and generally decrease monotonically with depth. This depth dependence is relatively weak over George’s Bank and the Scotian Shelf while quite strong over the tail of the Grand Banks, for example, near-bottom currents are about 50 % weaker than surface currents. The influence of tidal currents is clear at all three locations and is particularly strong over George’s Bank. Extreme currents are also generally stronger in fall–winter than in spring–summer.

5 Physical interpretation of extreme current speeds

The distribution and magnitudes of extreme non-tidal currents calculated in Sect. 3 are now interpreted by taking into account variability about the mean current speed pattern

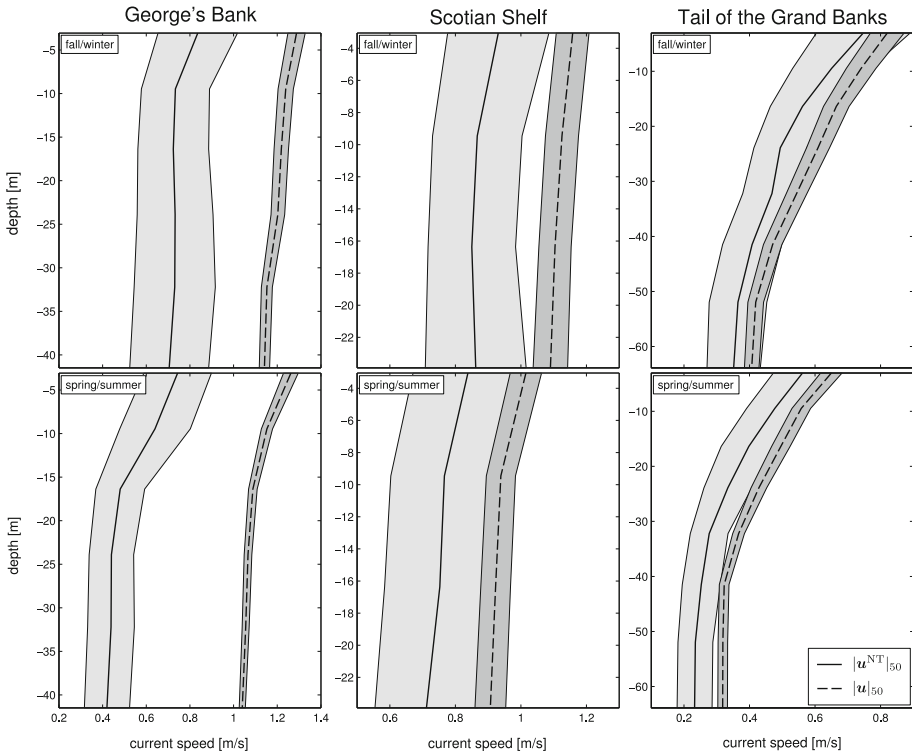


Fig. 8 Extreme current depth profiles at several locations with a return period of 50 years. The locations are on George’s Bank (*left*), the Scotian Shelf (*center*), and the tail of the Grand Banks (*right*). The locations are shown in Fig. 1. The 50-year extreme current speed was estimated in the same way as for Fig. 7. Results for fall–winter are shown in the *upper panels*, and results for spring–summer are shown in the *lower panels*. *Shaded areas* indicate the 95 % confidence intervals. The bathymetry along each transect is shown in the *lower panels*

(Sect. 5.1), Ekman currents due to extreme surface winds (Sect. 5.2), and the steering of flow along lines of constant bathymetry (Sect. 5.3).

5.1 The role of the mean current speed

In some regions, extreme surface and near-bottom currents are strongly dependent on the mean surface and near-bottom current speeds respectively. This is clear by comparing the spatial patterns of $|\mathbf{u}^{NT}|$ (Fig. 2) with $|\mathbf{u}^{NT}|_{\max}$ (Fig. 3). The extreme current speeds are large along the paths of three major current systems in the study region (i.e., the Gulf Stream, the North Atlantic Current and the Labrador Current). However, some regions also exhibit large extreme currents where the mean current speed is very weak (e.g., shallow regions).

The role of the mean current speed is quantified by the ratio of the 50-year extreme current speed to the mean current speed, $|\mathbf{u}^{NT}|_{50}/|\mathbf{u}^{NT}|$, at each location. A map of this ratio (Fig. 9) shows where extreme currents are due to significant variability about the mean (high values) and where extreme currents are largely controlled by the mean itself (low values). At the surface and within the main current systems (the Gulf Stream, the North

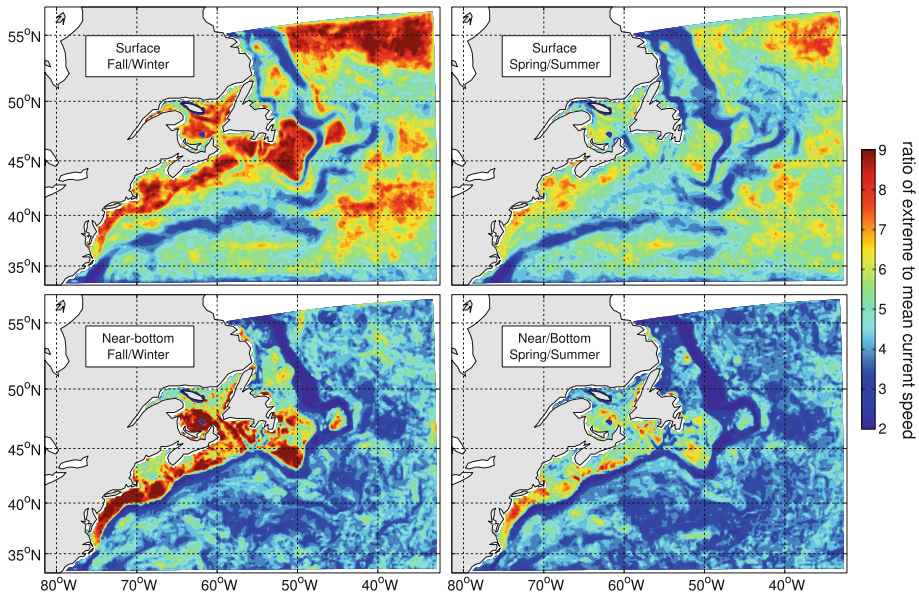


Fig. 9 Relative strength of extreme currents and the mean current speed. Filled contours indicate the ratio of the 50-year extreme current speeds to the mean current speed from the coupled model: $|\mathbf{u}^{\text{NT}}|_{50}/|\mathbf{u}^{\text{NT}}|$. The ratio is shown for fall–winter (*left*) and spring–summer (*right*) at the surface (*top*) and near the bottom (*bottom*)

Atlantic Current, and the Labrador Current), variability about the mean is relatively weak (i.e., extreme currents are on the order of or slightly larger than the mean current speed; Fig. 9, upper panels). However, in shallow regions, the extreme currents are up to 7 times stronger than the mean in spring–summer (upper right panel) and over 9 times stronger in fall–winter (upper left panel). The stronger fall–winter currents indicate that seasonal changes in wind variability may play a role in the seasonality of extreme current speeds. The role of surface wind stress will be explored in Sect. 5.2

Near the bottom, extreme current speeds are similar to the mean current speed in areas of steep topography (i.e., the continental slope). This may be due to the time-mean flow being strong and steered along isobaths in regions where the bathymetric gradient is large. The role of along- and cross-isobath extreme currents will be examined in Sect. 5.3. In addition, near-bottom currents are much stronger than the mean in shallow regions (over 10 times stronger in some regions) but of similar magnitude in deep water. This may be due to the influence of wind-driven currents being felt near the ocean bottom in shallow areas.

5.2 Extreme surface winds and Ekman currents

To examine the influence of surface wind forcing on the extreme currents, we estimate the wind-driven currents in a barotropic fluid forced by the extreme wind using Ekman theory (see “Appendix 4”). We assume the Ekman theory holds independently at each location and then calculate the Ekman currents at that location using the local 50-year extreme surface wind stress. Surface wind stresses in the zonal and meridional directions were estimated from CORE reanalysis 10 m wind (the model forcing, see “Appendix 1”) at each spatial grid point using the empirical drag coefficient of Large and Pond (1981). Their

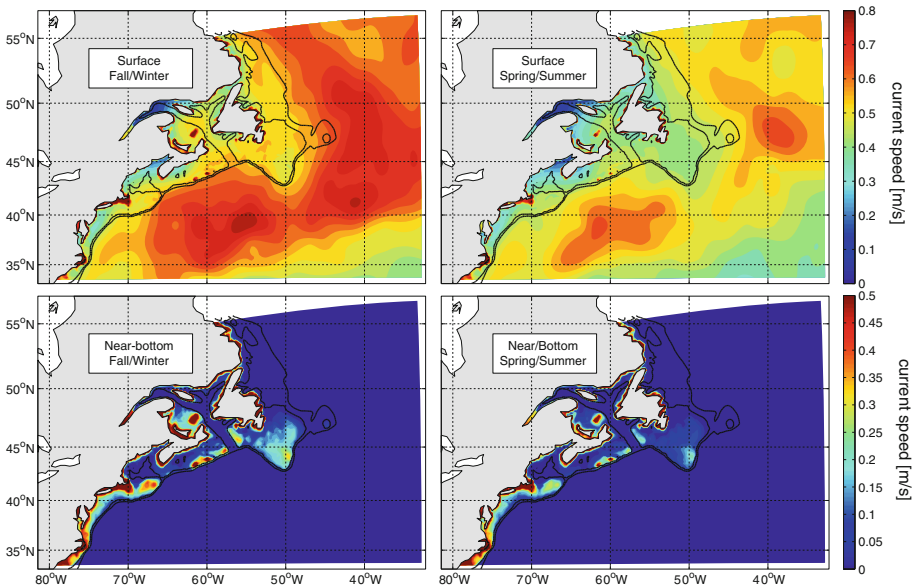


Fig. 10 Ekman currents due to extreme surface wind stress, $|\mathbf{u}^{\text{Ek}}|_{50}$. Ekman currents for fall–winter (left) and spring–summer (right) at the surface (top) and near the bottom (bottom) have been calculated from the theory outlined in Sect. 5.2 using the 50-year return period surface wind stress for each season. The thin black lines show the 200 and 1,000 m depth contours

formula provides a reasonable estimate of the drag coefficient for winds less than 40 m/s (Powell et al. 2003), which a preliminary extremal analysis on the surface winds shows is a reasonable assumption. An extremal analysis was then performed, and 50-year return period surface wind stress magnitudes were estimated from the fitted Type I distribution. The corresponding Ekman current speeds $|\mathbf{u}^{\text{Ek}}|_{50}$ at the surface (3 m depth) and near the bottom (center of bottom-most z -level at each grid point) were calculated using Eq. 14.

Ekman currents show a strong seasonal dependence (Fig. 10). At the surface, $|\mathbf{u}^{\text{Ek}}|_{50}$ are strongest south of Nova Scotia and east of the Grand Banks with peak speeds of 0.8 m/s in fall–winter and 0.65 in spring–summer (Fig. 10, upper panels). Fall–winter $|\mathbf{u}^{\text{Ek}}|_{50}$ are also noticeably stronger in shallow regions with speeds up to 0.6 m/s over parts of the Scotian Shelf, the Grand Banks, and the Gulf of St. Lawrence (compared with 0.4 m/s or less in spring–summer). Near the bottom, $|\mathbf{u}^{\text{Ek}}|_{50}$ are strongest in shallow water areas with fall–winter speeds up to 0.3 m/s on the Grand Banks and 0.5 m/s on parts of the Scotian Shelf and the Gulf of St. Lawrence (Fig. 10, lower panels). Fall–winter speeds are noticeably stronger than spring–summer speeds. Near the bottom, $|\mathbf{u}^{\text{Ek}}|_{50}$ are effectively zero in deep water regions. This is simply because the magnitude of the Ekman spiral decreases quickly with depth from the surface so that in deep water Ekman currents are very small near the bottom. The distribution and seasonality of near-bottom $|\mathbf{u}^{\text{Ek}}|_{50}$ is similar to that of the estimated near-bottom extreme currents ($|\mathbf{u}^{\text{NT}}|_{\text{max}}$ or $|\mathbf{u}^{\text{NT}}|_{50}$), especially in shallow areas (e.g., Fig. 4). Notable regions include the Tail of the Grand Banks, the Scotian Shelf break, St. Pierre Bank, and the waters surrounding Cape Breton Island and Prince Edward Island.

The $|\mathbf{u}^{\text{Ek}}|_{50}$ are weaker than the $|\mathbf{u}^{\text{NT}}|_{50}$. In some regions, this is because the $|\mathbf{u}^{\text{NT}}|_{50}$ arise through a combination of variability about the mean in addition to wind-driven Ekman currents. However, many assumptions have been made in the formulation of this model

that may underestimate the Ekman currents. We have assumed a constant vertical mixing coefficient, the functional forms used to calculate δ_E and μ are approximations, and the dynamical model has been applied independently at each location. We have also assumed steady state although this should, if anything, lead to an overestimation of wind-driven currents. Nonetheless, it is encouraging to find that the geographic pattern of $|\mathbf{u}^{\text{Ek}}|_{50}$, especially near-bottom currents, is similar to the pattern of extreme currents (e.g., Figs. 3 or 4) particularly that part which is not related to the mean flow.

5.3 Bathymetric steering of flow

Ocean currents are strongly constrained by topography, and here, we will examine the relative strength of along- and cross-isobath extreme currents. First, the along- and cross-isobath directions must be defined at each location. To do this, the bathymetry is first smoothed to remove high wavenumber variability with a uniform 7×7 matrix (an average size of 1.8° longitude by 1.1° latitude) whose elements sum to one. Then, the gradient of the smoothed bathymetry is calculated. From the gradient, unit vectors are defined indicating the directions along and across lines of constant bathymetry. Then, u and v produced by the coupled model are projected onto these vectors to yield the along- and cross-isobath currents. It should be noted that the along- and cross-isobath vectors are well defined in areas of steep topography, such as at the continental slope, but not in flatter areas such as the continental shelves and deep ocean.

Extreme along- and cross-isobath currents with 50-year return periods are calculated using the same technique as in Sect. 3 (not shown). At the surface, along-isobath extreme currents are dominant along the continental slope; elsewhere, they are not significantly different from cross-isobath currents. Near the bottom, on the other hand, along-isobath extreme currents dominate nearly everywhere except the edge of the Gulf of Maine. This is especially true along the continental slope where cross-isobath extreme currents are virtually zero. This analysis confirms that extreme currents over steep topography are strongest along lines of constant bathymetry as expected.

6 Summary and discussion

A methodology based on the extremal analysis and Monte Carlo methods used in this study to estimate long return period extreme current speeds from short record numerical model results was presented in this study. The three-dimensional 17-year non-tidal currents produced by a coupled ocean-ice model and barotropic tidal currents produced by Web-Tide were used to estimate and map 50-year extreme current speeds in the northwest Atlantic. First, the time-mean current speeds at the surface and near the bottom, $|\overline{\mathbf{u}^{\text{NT}}}|$, were mapped and shown to be consistent with observations (see also Urrego-Blanco and Sheng 2012). Maximum simulated non-tidal currents at the surface and near the bottom, $|\mathbf{u}^{\text{NT}}|_{\text{max}}$, over the 17-year hindcast period were then mapped, and seasonal changes were examined by performing the analysis independently on fall–winter and spring–summer. The $|\mathbf{u}^{\text{NT}}|_{\text{max}}$ provide estimates of the 17-year extreme current speeds. It was shown that $|\mathbf{u}^{\text{NT}}|_{\text{max}}$ is high in regions where $|\overline{\mathbf{u}^{\text{NT}}}|$ is also high (e.g., the Gulf Stream, the North Atlantic Current, the Labrador Current, the shelf break) and in shallow regions (e.g., the Grand Banks, the Scotian Shelf, the Gulf of St. Lawrence). It was also shown that there is strong seasonality with $|\mathbf{u}^{\text{NT}}|_{\text{max}}$ generally higher in fall–winter than in spring–summer.

We then estimated extreme currents with return periods longer than 17 years using the extremal analysis method. The performance of the method (i.e., fitting the Type I distribution to annual maxima) was demonstrated with long sea level records at Wakkanai (Japan) and Halifax (Canada). It was shown that extreme sea levels with long return periods (up to 100 years) can be predicted with only the first 17 years of hourly data. Using a Monte Carlo method, it was then shown that when tides play a significant role (i.e., in the Halifax record), they can be used to provide more accurate estimates of extreme sea levels with long return periods.

Extreme current speeds with 50-year return periods at the surface and near the bottom, $|\mathbf{u}^{\text{NT}}|_{50}$ and $|\mathbf{u}|_{50}$, were estimated from the 17-year NT coupled model run and predictions of tidal currents using the extremal analysis and Monte Carlo techniques described in “Appendices 2 and 3”. In this way, extreme current speeds with return periods longer than the length of the model prediction record were estimated. Both $|\mathbf{u}^{\text{NT}}|_{50}$ and $|\mathbf{u}|_{50}$ were mapped for the northwest Atlantic and plotted along three transects and as a function of depth for three locations. The extreme currents were interpreted taking into account the mean current speed, wind-driven currents, and the steering of flow along bathymetry.

The extreme current speeds exhibit a complex geographic pattern. This pattern is largely consistent with Wu et al. (2011) in the vicinity of the Grand Banks. This pattern can be explained as follows. Extreme currents tend to be oriented along lines of constant bathymetry and large along the continental slope, especially near the bottom. In deep water, extreme currents are typically weak near the bottom, and at the surface, they are dominated by the time-mean current speed (i.e., the main current systems such as the Gulf Stream). In shallow areas, extreme currents can be explained in large part by simple wind-driven Ekman currents that vary seasonally: fall–winter currents are generally much stronger than spring–summer currents. In addition, tidal flow can significantly affect the magnitude of extreme currents in shallow areas. This is especially true in tidally dominant areas such as George’s Bank.

The methodologies used in this study are limited in the following ways. First, the non-tidal currents produced by the coupled model may not accurately represent realistic conditions. The model resolution is not fine enough to resolve variability on small scales, that is, on the order of an oil platform or a pipeline. Additionally, the atmospheric forcing may not accurately reflect extreme atmospheric states. The resolution of the atmospheric reanalysis is marginally eddy-resolving and so may not properly resolve intense storm systems. This has most likely led to an underestimate of extreme currents especially at the surface during intense storms. Second, the statistical model has several limitations. We are predicting 50-year extreme currents with only 17 years of current predictions, and the extrapolation introduces additional uncertainty in the estimates of return speeds. In tidally dominant areas, this uncertainty is reduced somewhat although we have made the extra assumption that tidal and non-tidal variabilities are independent of each other. Finally, near-bottom currents have simply been taken as the center of the lowest model z -level. Some care must be taken when interpreting the pattern of extreme near-bottom currents, as in shallow regions, they may be a few meters from the bottom while in the deep, they are up to 125 m from the bottom.

It is encouraging to find that, despite the limitations described above, the distribution and magnitude of long return period (i.e., 50 years) extreme currents can be realistically estimated given only a short record length (i.e., 17 years). Future work should focus on more realistic predictions of northwest Atlantic currents. For example, the ocean circulation model could be run at a higher resolution thereby better resolving eddies and other

physical processes that may lead to extreme current speeds. The increased model run-time and data storage requirements of such a model run were beyond the scope of the current study. Also, if the atmospheric forcing reanalysis was performed at a higher spatial resolution [less than ~ 100 km, e.g., Hohenegger and Schar (2007)] then storms could be fully resolved thus leading to more accurate ocean surface forcing for the ocean. Finally, the inclusion of fully baroclinic tidal predictions could lead to better predictions of extreme currents and their seasonal variations.

Acknowledgments The authors would like to thank Kyoko Ohashi for providing the code used to generate tidal current predictions. The work was also supported by The Lloyd's Register Educational Trust (The LRET), which is an independent charity working to achieve advances in transportation, science, engineering and technology education, training, and research worldwide for the benefit of all. The authors would also like to thank the anonymous reviewers for their constructive comments.

Appendix 1: Coupled ocean-ice shelf circulation model

The coupled ocean-ice shelf circulation model is based on version 2.3 of the Nucleus for European Modelling of the Ocean (NEMO) modeling system (Madec 2008). It is a primitive-equation, finite difference ocean circulation model with a free surface and z -coordinates in the vertical. The model also contains a two-category (ice and open water) dynamic-thermodynamic sea ice model (LIM2, Timmermann et al. 2005).

The model resolution in the horizontal is $\sim 1/4^\circ$ in longitude and $\sim 1/4^\circ \cos \phi$ in latitude where ϕ is latitude. There are 46 z -levels in the vertical, with the vertical grid spacing increasing from 6 m at the surface to 250 m at the lowermost z -level. The model bathymetry is taken from ETOPO2 (Smith and Sandwell 1997). The model time step is 2,400 s.

The subgrid-scale horizontal mixing for momentum and tracers is parameterized using a biharmonic friction with the Smagorinsky-like mixing coefficient that is flow-dependent and varies horizontally as a function of the grid size (Griffies and Hallberg 2000). The vertical subgrid-scale mixing is parameterized using the turbulent closure scheme of Gaspar et al. (1990).

The lateral boundary conditions are as follows. At the model closed boundaries, a free slip condition is applied with zero normal fluxes of momentum, temperature and salinity. At the three lateral open boundaries (northern, eastern and southern), the normal flow, temperature, and salinity fields are adjusted based on the adaptive open boundary condition (e.g., Stevens 1990; Marchesiello et al. 2001; Sheng and Tang 2003). To reduce seasonal bias and drift in the model, a combination of the spectral nudging method (Thompson et al. 2006) and the smoothed semiprognostic method (Sheng et al. 2001; Greatbatch et al. 2004) is used.

The model surface boundary forcing consists of 12-hourly shortwave and longwave radiation, 6-hourly wind speed, air temperature, and air-specific humidity at 10 m above the sea surface, and monthly precipitation (rain and snow). The surface forcing fields were obtained from the Common Ocean-ice Reference Experiment reanalysis (CORE). CORE was generated by combining and correcting a variety of reanalyses and data sources (Large and Yeager 2004), and it was prepared especially for use as forcing in ocean modeling experiments. The data are defined on a grid with a resolution of 2° and interpolated to the model time step and grid. Note that the model is not forced by variations in atmospheric pressure. The model calculates surface fluxes from bulk formulae using the atmospheric forcing and the predicted ocean state. The model is spun up from a state of rest, initialized from the climatological monthly mean hydrography of Geshelin et al. (1999), and integrated for 18 years from 1 January 1987. Only the model results in the last 17 years (1988–2004 inclusive) are used in this study.

The model has been validated (Urrego-Blanco and Sheng 2012) using current measurements from drifting buoys, climatological hydrographic data, satellite-based measurements of sea surface temperature, and an estimation of the regional geoid (calculated using GRACE and both terrestrial- and satellite-based altimetry data). The validation procedure showed that the model has skill in predicting the large-scale circulation pattern in the northwest Atlantic and its seasonal variability. The model reproduces well both the time-mean geostrophic and the time-mean ageostrophic currents as well as the transports of the Labrador Current and the Gulf Stream.

Appendix 2: Extremal analysis

The statistical modeling of extreme events has a long history (e.g., Gumbel 1958). The seminal work of Leadbetter et al. (1983) outlined the mathematical theory underpinning extremal analysis, and Coles (2001) provided a readable primer on its methodology. In practice, there are several ways of modeling extremes. For example, in the “block maxima” approach, one fits the generalized extreme value (GEV) distribution to a set of maxima taken over subsets of the data (e.g., daily maxima, annual maxima, etc). In the slightly more complex “peak over threshold” approach, one fits the generalized Pareto distribution to data values that are larger than a chosen threshold value. The fitted distribution can then be used to estimate extremes with return periods longer than the record length. For scalar oceanographic or meteorological variables, such as sea level, the most common form used is to model the probability distribution of annual maxima using the Type I (Gumbel) distribution. The Type I distribution is a special case of the GEV distribution and has only two parameters to be estimated.

This study fits the GEV and Type I distributions to current speed annual maxima. This method is relatively straightforward and is commonly used. The length of time over which the maxima are taken defined is typically 1 year but, as discussed later, can also be taken to be a season. The use of the GEV avoids the choice of an arbitrary threshold value (which the generalized Pareto distribution would require).

The extremal analysis techniques used in this study are outlined below. Consider a stationary sequence of random variables $\{\eta_t | t = 1, 2, \dots\}$. Many sequences of environmental variables are not stationary due to low-frequency variability such as seasonal cycles and interannual variations. However, if n is at least as long as the characteristic time scales of these variations (e.g., 1 year for seasonal variations) then the theory outlined here still holds (Coles 2001). Let M_n denote the maximum defined over a block of length n :

$$M_n = \max(\eta_1, \eta_2, \dots, \eta_n). \tag{3}$$

If the cumulative distribution of M_n converges as n tends to infinity then it converges to one of three types: Gumbel (Type I), Fréchet (Type II), or Weibull (Type III) (e.g., Coles 2001). These distributions can be conveniently combined by the generalized extreme value (GEV) distribution:

$$F_{\text{GEV}}(x) = \exp\left\{-\left[1 + \xi\left(\frac{x - a}{b}\right)\right]^{-\frac{1}{\xi}}\right\}, \tag{4}$$

where a is the location parameter, $b > 0$ is the scale parameter, and ξ is the shape parameter. For $\xi \rightarrow 0$, the GEV distribution converges to the Type I distribution often used in the analysis of extreme sea levels,

Table 1 Details of the tide gauge records. Tide gauge locations are indicated in Fig. 1

Tide gauge	Latitude	Longitude	Start	End	% Complete
Halifax, Canada	44°40'N	63°35'W	1/1/1920	8/9/2011	98.3
Wakkanai, Japan	45°25'N	141°41'E	2/4/1968	31/12/2010	98.9

$$F_I(x) = \exp\left[-\exp\left(-\frac{x-a}{b}\right)\right]. \tag{5}$$

The quantiles of the Type I distribution can then be transformed into return periods T_r using the equation:

$$T_r(x) = [1 - F_I(x)]^{-1}, \tag{6}$$

where T_r has units of n . For example, if n corresponds to 1 year (i.e., M_n are annual maxima) then T_r has units of years. The usual approach, and the one used in this study, is to estimate a and b from a set of observed annual maxima using maximum likelihood. From the estimated values of a and b , it is then possible to estimate return periods for return levels higher than the observed annual maxima.

This extremal analysis method will be illustrated using two long sea level records. Sea level records were used due to the lack of long records of current speed. Hourly time series of sea level were obtained from tide gauges in Halifax (Canada) and Wakkanai (Japan) from the Hawai'i Sea Level Center (see Table 1 for details such as time period covered and completeness; see gray circles in Fig. 1 for locations). The linear trend was removed from each series and the residual denoted η . The tidal component of each record, η^T , was calculated using the analysis package of Pawlowicz et al. (2002) with 68 tidal constituents. The non-tidal component of sea level η^{NT} is then inferred by decomposing sea level into a sum of tidal and non-tidal components: $\eta = \eta^{NT} + \eta^T$.

The annual maxima for η^{NT} and η from both sea level records is shown in Fig. 11 by solid and dashed lines respectively. These records were chosen because they are both relatively long (>40 years) and because Halifax is tidally dominant while Wakkanai is not tidally dominant (the ratio of the standard deviation of η^T to the standard deviation of η^{NT} is 3.78 for Halifax and 1.03 for Wakkanai). Tidal variations have a significant impact on maximum sea level at Halifax whereas tides play a very minimal role at Wakkanai.

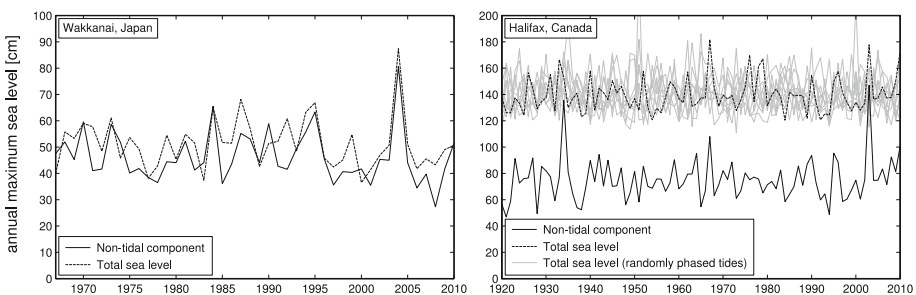


Fig. 11 Annual sea level maxima for Wakkanai (*left*) and Halifax (*right*). The annual maxima of η^{NT} are indicated by the *solid lines*, and the annual maxima of η are indicated by the *dashed lines*. Halifax annual maxima generated using the Monte Carlo approach described in “Appendix 3” are shown by *thin gray lines* (*right*)

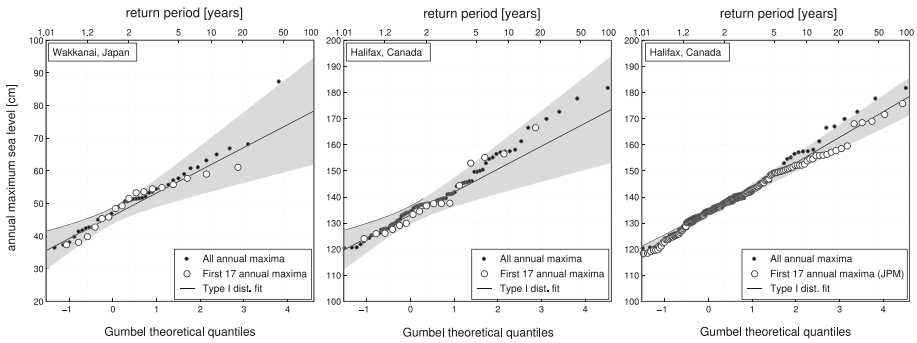


Fig. 12 Annual sea level maxima for Wakkanai (*left*) and Halifax (*center and right*) against the return period assuming a Type I (Gumbel) distribution. The observed annual maxima are indicated by the *small black circles (all panels)*, and annual maxima for the first 17 years are indicated by *open circles for Wakkanai and Halifax (left and center panels)*. The annual maxima using a Monte Carlo alternative to joint probability method (with $M = 10$) on the first 17 years at Halifax are indicated by *open circles (right panel)*. Linear fits based on the estimated parameters of the Gumbel distribution are shown as *solid lines with 95 % confidence limits shown as the shaded area*

The parameters of the GEV distribution (a , b , and ξ) for the annual maxima at both locations were estimated using maximum likelihood (e.g., Coles 2001). In both cases, the estimated value of ξ was not significantly different from zero at the 5 % significance level and so the Type I distribution is used instead of the GEV distribution. Plots of the annual maxima of η against the quantiles of the Type I probability distribution indicate a nearly linear relationship (Fig. 12, small black circles). Subsets consisting of the first 17 maxima were chosen from each series and plotted in the same way (Fig. 12, left and center panels, open circles). The parameters of the GEV distribution were estimated for these subsets and, as above, ξ was not significantly different from zero at the 5 % significance level leading to the use of the Type I distribution. The a and b coefficients allow one to predict beyond the 17-year return period, provided a linear relationship can be assumed to hold for longer return periods (Fig. 12, left and center panels, solid lines). In both cases, the linear relationship does a good job at predicting longer return period maxima. One exception is the largest maxima in the Wakkanai record that is poorly predicted by the linear relationship. This sea level maximum was due to a particularly large storm surge during Typhoon Songda in the Sea of Japan/East Sea in September 2004 (Kim et al. 2010). It is clear that, at least for these sea level records, extreme sea levels with long return periods (e.g., 100 years) can be predicted from a short subset of the data (e.g., 17 years).

In some regions, tides make up a significant proportion of the total variability and so they must be taken into account when estimating extremes. Tides are deterministic and can often be predicted to a high degree of accuracy using a tidal model. The joint probability method (JPM) has been developed to include tides and give reliable predictions of extreme events out to 100 year return periods or more with only a few years of non-tidal observations (Pugh and Vassie 1980; Tawn and Vassie 1989; Tawn 1992). The main advantage of JPM is that it takes into account the fact that non-tidal extrema may occur during different phases of the tide. An extension of JPM for bivariate variables was explored by Pugh (1982), and three methods were suggested for the application of JPM to ocean currents: (1) the JPM is applied to total current speed, (2) the bivariate variable is projected along particular directions and JPM is applied along each direction independently, or (3) the JPM is applied directly to the two-dimensional probability density. We will take a

slightly different approach that, although conceptually similar to JPM, is based on a Monte Carlo algorithm (see “Appendix 3”). The Monte Carlo method is illustrated for Halifax sea level where tidal variations are very strong. Halifax η^{NT} for the first 17 years was repeated 10 times with random start-time tides added to each replicate (i.e., Eq. 8 with $M = 10$). Each 17-year tide series was generated by taking a 17 year subset of η^T with a start time randomly chosen within the first 18.6 years (one nodal period). Concatenating the 17 replicates results in a record length of 170 years and the annual maxima shown in Fig. 11 (thin gray lines). Maximum likelihood was used to estimate a , b , and ξ from these annual maxima, and the use of the Type I distribution was again justified (at the 5 % significance level). A plot of the annual maxima against the return periods assuming a Type I distribution (Fig. 12, right panel, open circles) indicates a nearly linear relationship. The important point is that the annual maxima were calculated using only 17 years of the Halifax record and knowledge of the tidal cycle, and they provide reasonable estimates of centennial return levels (Fig. 12, right panel, solid lines).

Appendix 3: A Monte Carlo form of the joint probabilities method

The joint probabilities method (JPM) was developed to extract reliable return periods for extreme sea levels over long periods by including the effect of tides (Pugh and Vassie 1980; Tawn and Vassie 1989). If η_t is decomposed as

$$\eta_t = \eta_t^{NT} + \eta_t^T, \tag{7}$$

where η_t^T is the tidal component of η_t and η_t^{NT} is the non-tidal component, then the joint probability density is estimated by convolving the histograms of η_t^T and η_t^{NT} . From this estimated pdf for η_t it is possible to estimate extreme values for return levels much larger than the highest observed sea level if the tides are dominant. If the tidal and non-tidal components are not independent then it is not possible to separate the two as in Eq. 7 and convolve their probability distributions.

In this study, we used a simple Monte Carlo approach for including the effect of tides that is based on, and is equivalent to, the JPM. In essence, we generate new realizations of total currents (the sum of the tide and non-tidal components) by randomly changing the time lag between the tidal and non-tidal components of flow. This is performed by repeating the non-tidal component M times and each time adding a tidal component with a randomly chosen time lag relative to the non-tidal component:

$$\eta_{t+(m-1)N} = \eta_t^{NT} + \eta_{t-d_m}^T, \tag{8}$$

for $t = 1, 2, \dots, N$ N is the length of η_t^{NT}) and $m = 1, 2, \dots, M$. The $\{d_m | m = 1, 2, \dots, M\}$ are random integers selected from the hours in a full 18.6 year nodal cycle of the tide. The series η_t is now of length NM instead of N and is subject to the Gumbel-type analysis described above.

This method can be applied to current speed as follows. First, note that current speed cannot be decomposed as in Eq. 7, and instead, we work with the individual components:

$$u_t = u_t^{NT} + u_t^T \tag{9}$$

$$v_t = v_t^{NT} + v_t^T. \tag{10}$$

Then, the random coloration of tidal and non-tidal extrema (Eq. 8) is performed independently on u_t and v_t before recombining into total current speed $|\mathbf{u}_t| = \sqrt{u_t^2 + v_t^2}$.

Appendix 4: Ekman theory

The steady state Ekman theory can be expressed as

$$ifU_e = \frac{\partial}{\partial z} \left(\mu \frac{\partial U_e}{\partial z} \right), \tag{11}$$

where f is the Coriolis parameter, $U_e = u + iv$ combines the zonal and meridional velocity (u and v respectively) into a complex-valued variable ($i = \sqrt{-1}$), and μ is the vertical mixing coefficient (e.g., Kundu 1990). Equation 11 is subject to the following boundary conditions:

$$\mu \frac{\partial U_e}{\partial z} = \frac{\tau^s}{\rho_0} \quad \text{at } z = 0 \quad (\text{surface}) \tag{12}$$

$$\mu \frac{\partial U_e}{\partial z} = rU_e \quad \text{at } z = -H \quad (\text{bottom}), \tag{13}$$

where $\tau^s = \tau_r^T + i \tau_y^s$ is the surface wind stress, ρ_0 is the fluid density, and r is the bottom friction coefficient. Density ρ_0 is taken to be a typical value of 1024 kg/m^3 and the bottom friction coefficient r is taken from the model configuration to be $4 \times 10^{-4} \text{ m/s}$. In the case of constant μ , the solution is

$$U_e = \alpha_1 \frac{\cosh((1+i)(H+z)/\delta_E) + \alpha_2 e^{-i\pi/4} \sinh((1+i)(H+z)/\delta_E)}{\sinh((1+i)H/\delta_E) + \alpha_2 e^{-i\pi/4} \cosh((1+i)H/\delta_E)}, \tag{14}$$

where $\alpha_1 = \tau^s \delta_E e^{-i\pi/4} / \sqrt{2} \mu \rho_0$, $\alpha_2 = r \delta_E / \sqrt{2} \mu$, and δ_E is the Ekman depth. The Ekman depth and vertical mixing coefficient are calculated using the formulas $\delta_E = 0.1 \sqrt{\tau^s / \rho_0} / f$ and $\mu = \delta_E^2 f / 2$ respectively (Csanady 1982). (Note there is an implicit assumption that μ depends on wind speed.)

References

Bernier N, Thompson K (2006) Predicting the frequency of storm surges and extreme sea levels in the northwest Atlantic. *J Geophys Res* 111(C10):C10,009

Bernier N, Thompson K, Ou J, Ritchie H (2007) Mapping the return periods of extreme sea levels: allowing for short sea level records, seasonality, and climate change. *Global Planet Change* 57(1–2):139–150

Carter D, Loyens J, Challenor P (1987) Estimates of extreme current speeds over the continental slope off Scotland. Institute of Oceanographic Sciences, Report 239 143

Coles S (2001) An introduction to statistical modeling of extreme values. Springer, Berlin

Coles S, Walshaw D (1994) Directional modelling of extreme wind speeds. *Appl Stat* 43(1):139–157

Cook N (1985) The designer’s guide to wind loading of building structures. Part 1: background damage survey, wind data and structural classification. Building Research Establishment, Garston and Butterworths, London

Csanady G (1982) Circulation in the coastal ocean. Springer, Berlin

Dixon M, Tawn J, Vassie J (1998) Spatial modelling of extreme sea-levels. *Environmetrics* 9(3):283–301

Gaspar P, Grégoris Y, Lefevre J (1990) A simple eddy kinetic energy model for simulations of the oceanic vertical mixing: tests at station Papa and long-term upper ocean study site. *J Geophys Res* 95(C9):16179–16193

Geshelin Y, Sheng J, Greatbatch R (1999) Monthly mean climatologies of temperature and salinity in the western North Atlantic. *Can Data Rep Hydrogr Ocean Sci. Fisheries and Ocean Canada* 153

Greatbatch R, Sheng J, Eden C, Tang L, Zhai X, Zhao J (2004) The semi-prognostic method. *Cont Shelf Res* 24(18):2149–2165

- Griffies S, Hallberg R (2000) Biharmonic friction with a Smagorinsky-like viscosity for use in large-scale eddy-permitting ocean models. *Mon Weather Rev* 128(8):2935–2946
- Griffiths C (1996) Extreme residual current speeds upon the UK continental shelf. Health and safety executive offshore technology report, OTH94/437 43
- Gumbel E (1958) *Statistics of extremes*. Columbia University Press, New York
- Hennessey J (1977) Some aspects of wind power statistics. *J Appl Met* 16(2):119–128
- Hohenegger C, Schar C (2007) Atmospheric predictability at synoptic versus cloud-resolving scales. *Bull Am Meteorol Soc* 88(11):1783–1794
- Kim S, Matsumi Y, Yasuda T, mase H (2010) Mechanism of abnormal storm surges after passage of typhoons around west coasts of the sea of Japan. *J Jpn Soc Civil Eng Ser B2 (Coast Eng)* 66(1):221–225
- Kundu P (1990) *Fluid mechanics*. Academic Press, London
- Large W, Pond S (1981) Open ocean momentum flux measurements in moderate to strong winds. *J Phys Oceanogr* 11(3):324–336
- Large W, Yeager S (2004) Diurnal to decadal global forcing for ocean and sea-ice models: the data sets and flux climatologies. National Center for Atmospheric Research, Boulder
- Leadbetter M, Lindgren G, Rootzén H (1983) *Extremes and related properties of random sequences and processes*, vol 11. Springer, Berlin
- Loder J, Petrie B, Gawarkiewicz G (1998) The coastal ocean off northeastern North America: a large-scale view. *Sea* 11:105–133
- Lyard F, Lefevre F, Letellier T, Francis O (2006) Modelling the global ocean tides: modern insights from fes2004. *Ocean Dyn* 56(5):394–415
- Madec G (2008) NEMO ocean engine. Institut Pierre-Simon Laplace (IPSL), France
- Marchesio P, McWilliams J, Shepetchin A (2001) Open boundary conditions for long-term integration of regional oceanic models. *Ocean Model* 3(1–2):1–20
- Palutikof J, Brabson B, Lister D, Adcock S (1999) A review of methods to calculate extreme wind speeds. *Meteorol Appl* 6(02):119–132
- Pawlowicz R, Beardsley B, Lentz S (2002) Classical tidal harmonic analysis including error estimates in MATLAB using T_TIDE. *Comput Geosci* 28(8):929–937
- Powell M, Vickery P, Reinhold T (2003) Reduced drag coefficient for high wind speeds in tropical cyclones. *Nature* 422(6929):279–283
- Pugh D (1982) Estimating extreme currents by combining tidal and surge probabilities. *Ocean Eng* 9(4):361–372
- Pugh D, Vassie J (1980) Application of the joint probability method for extreme sea level computations. *Proc Inst Civ Eng Part 2(69):959–975*
- Sheng J, Tang L (2003) A numerical study of circulation in the western Caribbean Sea. *J Phys Oceanogr* 33(10):2049–2069
- Sheng J, Greatbatch R, Wright D (2001) Improving the utility of ocean circulation models through adjustment of the momentum balance. *J Geophys Res* 106(C8):16,711–16
- Smith W, Sandwell D (1997) Global sea floor topography from satellite altimetry and ship depth soundings. *Science* 277(5334):1956
- Stevens D (1990) On open boundary conditions for three dimensional primitive equation ocean circulation models. *Geophys Astrophys Fluid Dyn* 51(1–4):103–133
- Tawn J (1992) Estimating probabilities of extreme sea-levels. *Appl Stat* 41(1):77–93
- Tawn J, Vassie J (1989) Extreme sea levels: the joint probability method revisited and revised. *Proc Inst Civ Eng Part 2(87):429–442*
- Thompson K, Wright D, Lu Y, Demirov E (2006) A simple method for reducing seasonal bias and drift in eddy resolving ocean models. *Ocean Model* 13(2):109–125
- Timmermann R, Goosse H, Madec G, Fichefet T, Ette C, Dulière V (2005) On the representation of high latitude processes in the ORCA-LIM global coupled sea ice-ocean model. *Ocean Model* 8(1–2):175–201
- Urrego-Blanco J, Sheng J (2012) Interannual variability of the circulation over the eastern Canadian shelf. *Atmos Ocean*. doi:10.1080/07055900.2012.680430
- Wu Y, Tang C, Li M, Prescott R (2011) Modelling extreme storm-induced currents over the grand banks. *Atmos Ocean* 49(3):259–268
- Zwiers F (1987) An extreme-value analysis of wind speeds at five Canadian locations. *Can J Stat* 15(4):317–327